Research Article Vol. 2, No. 6 / June 2015 / Optica 523

Experimental access to higher-dimensional entangled quantum systems using integrated optics

Christoph Schaeff,[1,5] Robert Polster,[1] Marcus Huber,[2,3] Sven Ramelow,[1] and Anton Zeilinger[1,4,*]

[1]Faculty of Physics, University of Vienna, Boltzmanngasse 5, 1090 Vienna, Austria
[2]Universitat Autonoma de Barcelona, 08193 Bellaterra, Barcelona, Spain
[3]ICFO-Institut de Ciencies Fotoniques, 08860 Castelldefels, Barcelona, Spain
[4]Institute for Quantum Optics and Quantum Information (IQOQI), Austrian Academy of Sciences, Boltzmanngasse 3, 1090 Vienna, Austria
[5]e-mail: christoph.schaeff@univie.ac.at
*Corresponding author: anton.zeilinger@univie.ac.at

Received 16 March 2015; revised 24 April 2015; accepted 30 April 2015 (Doc. ID 236334); published 1 June 2015

Integrated optics allows for the generation and control of increasingly complex photonic states on chip-based architectures. Here, we implement two entangled qutrits—a nine-dimensional quantum system—and demonstrate an exceptionally high degree of experimental control. The approach, which is conceptually different to common bulk optical implementations, is heavily based on methods of integrated in-fiber and on-chip technologies and further motivated by methods commonly used in today's telecommunications industry. The system is composed of an in-fiber source creating entangled qutrit states of any amplitude and phase, and an on-chip integrated general Multiport enabling the realization of any desired local unitary transformation within the two qutrit nine-dimensional Hilbert space. The complete design is readily extendible toward higher dimensions with moderate increase in complexity. Ultimately, our scheme allows for complete on-chip integration. We demonstrate the flexibility and generality of our system by realizing a complete characterization of the two-qutrit space of higher-order Einstein–Podolsky–Rosen correlations.

OCIS codes: (270.0270) Quantum optics; (130.0130) Integrated optics.

http://dx.doi.org/10.1364/OPTICA.2.000523

1. INTRODUCTION

Higher-dimensional entangled quantum states are highly relevant for fundamental questions in quantum physics and have gained increasing practical relevance due to their distinguishing properties compared to qubit states [1–5]. Moreover, there is a wide range of open theoretical questions for quantum systems not composed of multiple qubits [6]. The reasons for the difficulty in implementing higher-dimensional systems are mainly technical in nature. In particular, when path-encoded photonic states are used, phase stability quickly becomes very challenging using a bulk optical approach traditionally used in many quantum optical experiments. Consequently bulk optical designs are restricted in their complexity, thereby hindering progress toward higher-dimensional quantum systems. Here, we choose a conceptually different experimental approach. We utilize recent progress within the area of optical telecommunication in management and automatization of high numbers of complex optical devices. In particular, we aim at combining state-of-the art optical fiber networks and integrated photonic circuit technology with methods of quantum optics. The latter has already proven successful in different quantum experiments utilizing various integrated photonic devices [7–13]. Eventually, an integrated optics approach allows for complete access to complex quantum systems with a high degree of flexibility and automatization, good scalability toward higher-dimensional realizations, as well as direct control over the parameters defining the quantum system. Reconfigurable integrated quantum circuits for qubits have been shown so far in a silica-on-silicon architecture [10]. We are not only going significantly beyond this work by demonstrating universal unitary operations in two local nine-dimensional Hilbert spaces, but thereby are also showing the scalabilty of our approach toward even higher-dimensional states. Moreover, we achieve interfacing our universal multiport chips with a maximally path-entangled qutrit source—something that we demonstrate here for the first time to our knowledge—and show how the source design, phase stabilization, and interfacing scale very favorably for extending it to higher dimensions. Finally, we enter a new wavelength regime for complex integrated quantum circuits by operating in the telecommunication band around 1550 nm. This makes our approach directly compatible to fiber-optic networks and quantum communication applications and is technologically highly promising, as this wavelength regime features extremely mature fiber technology and is the main focus of technological advancements in integrated optics. In the context of higher-dimensional quantum systems, higher-order nonlocal correlations between two (entangled) particles are of importance as they represent a

fundamental distinguishing property to the classical world [14]. However, controlled creation and transformation in addition to N outcome projective measurements of the higher-dimensional entangled system are required. All these requirements are met by our implemented system. We will present the concepts of our approach along with a first realization of a fully controlled and automated entangled two-qutrit nine-dimensional quantum system. The final setup allows us to completely map the two-qutrit correlation space and to compare it to theoretical predictions.

2. THEORY

A general quantum optical configuration is illustrated in Fig. 1. For $N = 2$, it represents the classic textbook case of a basic two-qubit ($N = 2$) quantum system. Generally, the system is composed of three components: the creation (S), transformation (U), and detection (D) of a quantum state. A source (S) creates two particles, each composed of N modes, a so-called quNit, forming the entangled state

$$|\psi_N\rangle = \sum_{k=1}^{N} A_k e^{\phi_k - \phi'_k} |kk\rangle. \quad (1)$$

After separation, each quNit A and B is transformed by a local unitary transformation (U):

$$|\psi_{N'}\rangle \rightarrow (U_A \otimes U_B)|\psi_N\rangle. \quad (2)$$

The experiment concludes with the measurement, e.g., single-photon detection of both quNits A and B corresponding to an underlying projective measurement,

$$P_{ab} = |a\rangle\langle a| \otimes |b\rangle\langle b|, \quad (3)$$

of the quantum state $|\psi\rangle$. The expectation value $\langle P_{ab}\rangle$ relates to the number of detected photon pairs and represents the measurement result.

Although for $N = 2$, Fig. 1 becomes a conceptually simple example, it has revealed a number of quantum effects with consequences ranging from theoretical insights to prospects of applications. Quantum entanglement, manifesting itself in so-called Einstein–Podolsky–Rosen (EPR) correlations, is the first example to name [15]. Interestingly, although different sets of EPR correlations exist in any dimension N, only for $N = 2$ does the number of different perfect correlations coincide with the number of all theoretically possible correlations [15,16]. Naturally, the question arises of what is to come for $N > 2$. In contrast to a qubit system, a single qutrit ($N = 3$) cannot be explained by noncontextual approaches [17]. For $N \geq 4$, infinite classes of symmetric beam splitters can exist with consequences for the observation of higher-order entanglement [15]. At $N = 6$, the question of the existence of a complete set of mutually unbiased basis is still unanswered [18]. Our motivation is to obtain experimental access to such quantum systems providing the basis for future tests and verifications of theoretical concepts.

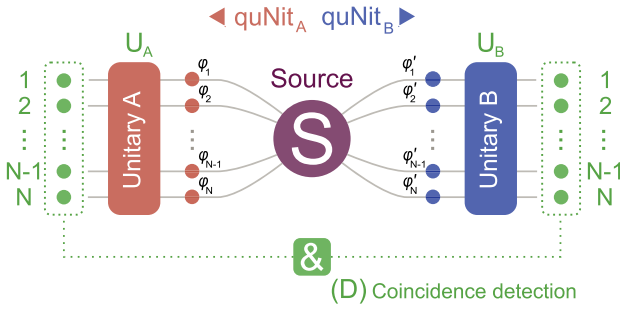

Fig. 1. Concept of an entangled two-quNit N^2-dimensional quantum experiment. A source (S) creates the path-encoded entangled two-quNits state. After separation, each quNit passes $N - 1$ phase shifters followed by a local unitary transformation (U). Eventually, the state is detected and coincidence detection events are recorded (D).

It is worthwhile mentioning that a particular experiment can be considered as one element within the full range of possible experiments covered by the general configuration in Fig. 1. In contrast, we do not aim toward a single predefined measurement but rather toward a general platform allowing for a great range and flexibility within the space of all possible experiments covered by the configuration in Fig. 1.

3. EXPERIMENTAL IMPLEMENTATION

In principle, a photonic quNit system can be encoded using any degree of freedom. However, physical and technical constraints pose a limit. Here, path encoding will be utilized. In some way, it may be considered as the most direct way of encoding quantum information into a system. Of immediate advantage is the possibility of near-perfect (experimental) separability of path-encoded modes via spatial separation. Additionally, there is no fundamental limit on the number of paths. Choosing path encoding as the starting point methods of on-chip and fiber optics offer exceptional mode and path control. The system is built using only integrated components and can be deconstructed into three parts: source (S), transformation (U), and detection (D), as illustrated in Fig. 1.

A. Source of Entangled Qutrits (S)

We have previously presented a scalable in-fiber source of path-encoded entangled quNits at telecom wavelengths [19]. It uses N nonlinear crystal waveguides to create photon pairs of same polarization but different wavelength centered around 1550 nm. All crystals are coherently pumped by a common 775 nm pump beam, split by a sequence of beam splitters. The result is a superposition of pair creation events occurring at one of the N crystals. This is followed by 100 GHz in-fiber filters separating and filtering each photon pair by wavelength (1551.7 nm, 1548.5 nm). A number of optical in-fiber devices ensure the matching of optical properties (spectrum, coherence, arrival time, loss, polarization), making all pair-creation events indistinguishable from each other. Thereby, an entangled two-quNit state is obtained. The main features of this design are its high brightness and quality of the entangled state, high robustness due to a fully fiber-integrated approach, and compatibility to standard path-encoded integrated optical circuits along with a low propagation loss and good scalability in complexity when increasing the dimension of the system. We have extended the source of two entangled qubits following the scheme previously presented in [19] to two entangled qutrits ($N = 3$).

B. Multiport (U)

The so-called general Multiport (MP) allows an experimenter to realize any unitary transformation defined by $N^2 - 1$ parameters. Here, it is realized using a combination of phase shifters and beam splitters. The setting of each optical device directly relates to a parameter of the unitary transformation. Depending on the phase

and reflectivity settings, any unitary transformation is realized [15,20]. In order to effectively manage the internal complexity of the device, we have chosen an integrated photonic implementation.

Light-guiding silica waveguides of low index contrast ($\Delta \approx 1.5\%$) optimized for C-band operation (cut-off wavelength $\lambda_{\text{cutoff}} \approx 1450$ nm) are used. Waveguide modes closely match to the mode of a single-mode fiber at 1550 nm. Beam splitters are realized by evanescent coupling of two waveguides brought to proximity. Two 50/50 beam splitters form a Mach–Zehnder interferometer, with phase shifters in each arm representing a tunable beam splitter of arbitrary reflectivity. Phase shifters are realized via the thermo-optical effect using heating electrodes above the photonic circuit on top of the cladding layer. Trenches are etched around phase shifters to ensure high thermal insulation. All phase shifters are permanently connected using a custom electronic probe card mounted from the top onto the chip. The 3×3 MP circuit features six beam splitters and 21 phase shifters (not all theoretically required). The chip is thermally stabilized, ensuring optimal operating temperature. Total insertion loss, including in- and out-coupling, amounts to approximately 9 dB. The length of the 3×3 MP circuit is 6.5 cm at a waveguide spacing of 250 μm. The device is permanently packaged to standard optical fibers and electric connectors serving as a convenient optical and electrical interface. The complete housing has a size of less than 10 cm × 5 cm × 5 cm. Any unitary transformation entered by the user is automatically realized by a computer program translating the entered unitary matrix down to independent heating currents. Switching the MP to unitary transformations requires $t < 100$ ms. However, we expect the actual switching time to be significantly lower. Comparable silica circuits based on the thermo-optical effect have reached switching times on the order of 1 ms [21]. For a single silica switch, switching times on the order of 50 μs have been reported [22]. Nonetheless, the current switching time is negligible compared to common single-photon detection integration times on the order of 10 s. Therefore, switching the MP currently does not limit the experimental procedures in any way. We have thus not focused further on the issue. Due to the high level of control and automation, the MP can be considered a black-box device. Any unitary transformation entered by the experimenter is automatically realized.

C. Detection (D)

The outputs $a = i$ of qutrit A are detected by a free-running, high-performance, low-noise single-photon detector. A detection event will simultaneously trigger three single-photon detectors at output modes $b = I, II, III$ of qutrit B, opening the detection window for 2.5 ns. A detection event at B will be treated as one detected photon pair, leading to the count rate CC_{ab}. Output modes $(a, b) = (i, I), (i, II), (i, III)$ are measured simultaneously, yielding the corresponding probabilities of joint detection $P_{ab} \propto CC_{ab}$. Generally, CC_{ab} depends on all parameters defining the quantum system. In particular, the relative phases $CC_{ab} = CC_{ab}(\phi_1 - \phi_1', \phi_1 - \phi_1')$ are of importance. Note that for $a \neq i$, no physical detectors are necessary as explained later.

4. PREPARATION AND PERFORMANCE

The complete setup is illustrated in Fig. 2. All free parameters defining the quantum system are under experimental control. The **Source (S)** handles the creation of the entangled state:

- The pump power within each crystal controls all amplitudes A_1, A_2, A_3. Similar to the splitting ratios, the coherence of the pump beam could be controlled by inserting fiber delay lines for other types of quantum states. Here, without exception, we set the amplitudes to an equal superposition state $A_1 = A_2 = A_3 = \frac{1}{\sqrt{3}}$.

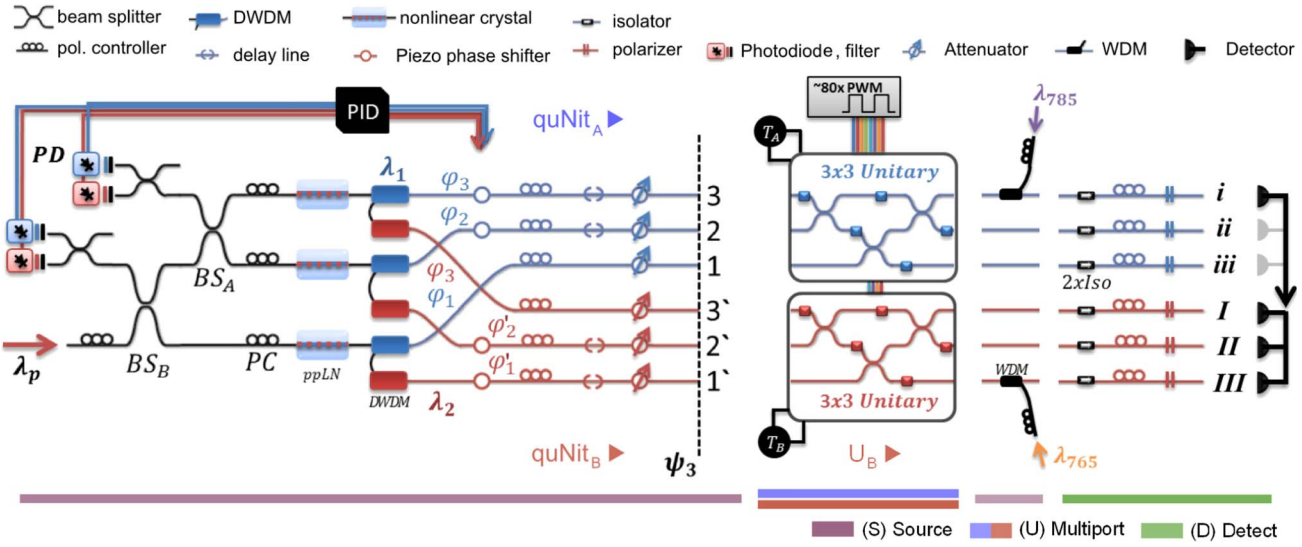

Fig. 2. Illustration of the experimental arrangement. All components are directly interfaced via standard optical fiber connectors or directly spliced together for minimal optical loss. (S) A superposition between N photon pair creation events is produced by coherently pumping N nonlinear crystals. For each channel, the photon pair is separated by wavelength followed by a number of in-fiber components ensuring matching optical properties. Eventually, an entangled two-qutrit state is obtained. Using the interference signal of reference light ($\lambda_{765}, \lambda_{785}$) inserted backward into the system, a proportional integral derivative (PID) controller is actively stabilizing all phases of the in-fiber system. (U) Each qutrit is directly connected to the packaged MPs performing any arbitrary local unitary transformation onto the system. (D) Eventually, using single-photon detectors, the measurement concludes when pair-detection events are recorded.

• An active PID feedback mechanism ensures complete control and stabilization of all phases $\phi_1, \phi_1', \phi_2, \phi_2', \phi_3, \phi_3'$ of the entangled state (details in [19]).

The final state should approximately assume the form

$$|\psi_N\rangle = \sum_{k=1}^{N} A_k e^{\phi_k - \phi_{k'}} |kk\rangle. \quad (4)$$

Two **Multiport (U)** devices are connected to qutrit A and B, realizing local transformations taking the form

$$U_{A/B} = \begin{pmatrix} (a/b)_{11} & (a/b)_{12} & (a/b)_{13} \\ (a/b)_{12} & (a/b)_{22} e^{\phi_{22}} & (a/b)_{23} e^{\phi_{23}} \\ (a/b)_{13} & (a/b)_{23} e^{-\phi_{23}} & (a/b)_{33} e^{\phi_{33}} \end{pmatrix}, \quad (5)$$

with a total of 16 real parameters. Each MP can be independently configured to realize different local unitary transformations within SU(3).

Single-photon detection (D) completes the experiment. A unitary transformation U_{Proj} of the detection basis allows for the realization of any projective measurement. Thus, if a certain projective measurement is desired, the MP is set to include the appropriate transformation U_{Proj} on top of the transformation of the particular experiment $U \rightarrow U U_{\mathrm{Proj}}$. The existence of noise in the system is dominantly a result of accidental coincidence detection events due to a finite detection time window, where the coincidental clicks do not originate from a produced photon pair. Noise of this type can be quantified and is subtracted for all following measurements and quantities if not stated otherwise. Due to the property of the noise, it can be reduced by decreasing the created pair rates per crystal.

In anticipation of future experiments, instead of measuring a particular fixed set of relative phases $CC_{ab}(\phi_1 - \phi_1', \phi_1 - \phi_1')$, we choose a different approach: all relative phases are scanned stepwise within $0, \ldots, 2\pi$. Thereby, a complete map of the correlation space CC_{ab} is obtained. Afterward, any particular set of phases can be extracted based on a fit obtained from the complete scan of the space. Any measurement herein will utilize this approach.

Before continuing with more complex measurements in the full two-qutrit quantum space and for a better understanding of the system, we present some more straightforward measurement results:

• The previous two-qubit source achieved a state fidelity of $F = (99.44 \pm 0.06)\%$ [19]. The current qutrit system involves three two-qubit subspaces. Using the MP, all subspaces A, B, C can be accessed and characterized in a similar way (see [19]). Compared to the theoretically expected perfect state, we reach a state fidelity of $F_A = (96.22 \pm 0.73)\%$, $F_B = (93.33 \pm 0.88)\%$, $F_C = (96.86 \pm 0.69)\%$.

Naturally, the resulting fidelity is lower than the optimized qubit source. The qutrit system has not been optimized for measurement in a qubit subspace. In fact, the remaining part of the unitary space the MP cannot realize are perfect qubit transformations excluding one mode from any interaction. Consequently, any measurement using such transformations will be of less quality when assuming a perfect transformation. We have not further addressed this issue since qubit subspaces will be of little interest building a qutrit system. In any case, a sufficient quality of the state is achieved.

• Extrapolating the two qubit subspace measurements to the full Hilbert space, one immediately reveals the potential of the MP to sustain and manipulate genuine higher-dimensional entanglement. With the achieved subspace fidelities and an equal population of every path, we can use the results of Ref. [6] in order to show that the MP is capable of maintaining a genuine qutrit-entangled state. We find a corresponding lower bound on the number of "e-bits", i.e., entangled bits; the universal currency of bipartite entanglement of $E_{oF}(\rho) \geq 1.15$, which is significantly above the maximum obtainable value of an entangled qubit system as qubits can never encode more than one e-bit. Furthermore, reaching the upper bound of qubits would require perfectly prepared pure states and noiseless channels and measurements.

5. RESULTS

For a first demonstration, we perform a complete automated characterization of the higher-order two-qutrit EPR correlations [15].

For its observation, a maximally entangled two-qutrit state is required along with two three-dimensional beam splitters and local three-outcome measurements, pointing at the difficulty in observing higher-order correlations.

Both MPs are used to realize the extension of the balanced beam splitter to higher dimensions, the so-called Bellport, taking on the form [15]

$$U = \frac{1}{3} \begin{pmatrix} 1 & 1 & 1 \\ 1 & e^{\frac{2\pi}{3}} & e^{\frac{\pi}{3}} \\ 1 & e^{\frac{2\pi}{3}} & e^{\frac{2\pi}{3}} \end{pmatrix} \otimes \begin{pmatrix} 1 & 1 & 1 \\ 1 & e^{\frac{2\pi}{3}} & e^{\frac{\pi}{3}} \\ 1 & e^{\frac{2\pi}{3}} & e^{\frac{2\pi}{3}} \end{pmatrix}. \quad (6)$$

Note that the matrix elements of the Bellport may be viewed as elements of the discrete Fourier transformation (FT) of the inputs. Thus, if a particle enters one input it will exit the device at any unpredictable output with equal probability (in analogy to the FT of a delta peak). However, in contrast to classical physics, quantum correlations of two entangled particles, each entering a similar device, allow for the imposition of certain constraints and predictions onto the particle's exit mode.

For a detailed analysis, we measure a complete map of the two-qutrit correlation space $CC_{ab}(\phi_x, \phi_y)$ spanned by the two relative phases. Iteratively, ϕ_x is set to 0°, 10°, 20°, …, 360° in steps of 10°. For each value of ϕ_x, ϕ_y is measured in 30 steps between 0 and 2π. A fit $f(\phi_y)$ is applied to the recorded correlation signal $CC_{ab}|_{\phi_x}^{\phi_y \in (0,2\pi)}$ while ϕ_x is kept constant. Eventually, the resulting 36 fitted signals $f(\phi_y)$ are displayed for each ϕ_x and for every detector combination $\{(i, I), (i, II), (i, III)\}$ slice by slice in Fig. 3. A total of 1080 different measurement points with 8 s integration time have been recorded. At maximum, a coincidence count rate of around 600/8 s at a SNR ≥ 10 is achieved. The experiment was calibrated, controlled, stabilized, and performed fully automatically.

The measurement results (Fig. 3) reveal excellent agreement with theoretical predictions. Notably, given the experimental resolution, even the minima are clearly visible. Some particular observations are listed below:

• The correlation pattern (Fig. 3) exhibits three distinct correlation maxima at the predicted phase setting (colored dots in Fig. 3) [15]. For example, if detector combination (i, I) exhibits a maximum, the other two combinations (i, II) and (i, III) show a minimum in detected coincidences.

• In principle, the number of possible correlations between detector combinations equals $N! = 6$ [15]. However, given the experimental resolution (Fig. 3), we observe three correlation

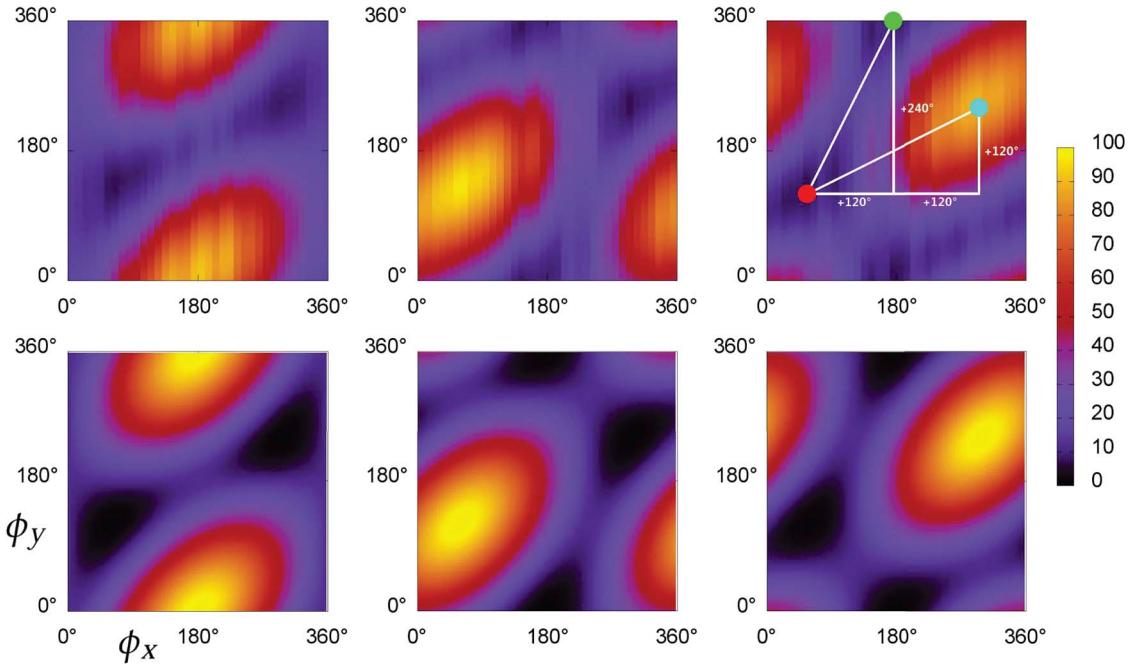

Fig. 3. A full scan of the two-qutrit correlation space spanned by the two relative phases $CC_{ab}(\phi_x, \phi_y)$ is performed (top row) and compared to theoretical predictions (bottom row). Iteratively, ϕ_x is set to 0°, 10°, 20°, …, 360° in steps of 10°. For each value of ϕ_x, ϕ_y is measured in 30 steps between 0 and 2π. Eventually, a fit $f(\phi_y)$ is applied to the recorded correlation signal $CC_{ab}|_{\phi_x}^{\phi_y \in (0,2\pi)}$. The resulting 36 fitted signals $f(\phi_y)$ are displayed for each ϕ_x and for every detector combination $\{(i, I), (i, II), (i, III)\}$ slice by slice. The maximum coincidence count rates reach approximately 600/8 s at a SNR ≥ 10. The overlays of the top right picture are used to highlight special characteristics of the correlation space as described in the text. The experiment is calibrated, controlled, stabilized, and performed fully automatically.

maxima at three distinct phase settings equal to the system's dimension $N = 3$. The remaining $N! - N = 3$ possible correlations between detectors do not appear, as is expected from quantum theory [15].

- Examining the middle graph of Fig. 3, the maximum correlation appears at (60°, 120°) while minima appear at (180°, 360°) and (300°, 240°) (as illustrated by the arrows). The relative distance is given by (0°, 0°), (240°, 120°), and (120°, 240°), as expected.
- For a qubit beam splitter, a measurement of the second output is equivalent to a measurement of the first output plus an input phase offset of 180° [15,23]. Consequently, measuring a certain point (ϕ_x, ϕ_y) for all nine possible detector combinations should be equivalent to measuring the three points (ϕ_x, ϕ_y), $(\phi_x + 120°, \phi_y + 240°)$, and $(\phi_x + 240°, \phi_y + 120°)$ while recording only joint detection events between (i, I), (i, II), and (i, III). Figure 3 strengthens this assumption, which is the reason for the implemented detection scheme using only a single detector for qutrit A.
- The observed correlation pattern is similar to the expected classical interference pattern of a three-path Mach–Zehnder interferometer (MZI) as previously observed [24]. Here, the pattern is nonclassical: it becomes visible solely in coincidence detection. Local observation of single-detection events (ideally) does not exhibit any pattern and a photon will be observed with the same probability of 1/3 at any output.
- Three-path interference results in a higher phase sensitivity $S \propto |dI/d\phi|$ due to the existence of side lobes [24]. In order to reveal the effect within the two-particle correlation pattern, the output intensity I is replaced by the number of detected pairs and extracted from the measurement data. The maximal measured phase sensitivity averaged over the three measured detector combinations becomes

$$\overline{S} = (0.703 \pm 0.019)\ \text{rad}^{-1}. \quad (7)$$

The theoretical maximum sensitivity of three-path interference is given by $S_3^{\text{th}} \approx 0.782$. Compared to the qubit case with $S_2^{\text{th}} = \frac{1}{2}$, an increase in sensitivity by a factor of $\gamma = 1.41 \pm 0.04$ is achieved.

These observations demonstrate the good operation of the MP devices and the achievable purity of the input states. The fact that the whole correlation space is accessible also implies that any quantum information protocol that can be performed using entanglement and local unitary transformations is directly implementable with our setup.

In addition, we wish to highlight the scalability of the current system toward higher-dimensional quantum systems. The scalability of the source has been previously addressed [19]. While a detailed discussion would be beyond the scope of this article, we can provide a representative example of the power of integrated optics in the context of the MP design. The integrated Matrix Switch, a device used in the area of communication, redirects light entering one of N inputs to one of N outputs by a combination of tunable MZIs. Matrix Switches up to 32×32 in/outputs based on similar silica waveguide technology have been reported [25] featuring 2048 beam splitters, 2048 phase shifters, and 60 cm of total waveguide length integrated on a single chip at an insertion loss below 10 dB. In comparison, the Matrix Switch circuit structure is highly similar to a MP. In fact, in terms of device complexity, a 32×32 MP would require half the number of optical devices compared to the above Matrix Switch. Unfortunately, current-generation matrix switches are highly optimized, leading to a circuit design not usable as a MP.

Other designs [26] have a higher similarity to the MP, and we will address this issue in a separate article. An important aspect of interfacing a high-dimensional path-entangled source as ours with MP chips is the scaling of the resources for active phase stabilization. The method we have developed for the $N = 3$ case involves back-illuminating the complete beam path with two lasers of different wavelength injected into the output. The interference signal at two of the inputs for both lasers (four detectors in total, see Fig. 1) is then measured and used for stabilizing the phases of the fibers connecting the source and the MP chip. A careful analysis shows that scaling up this design would require only two more detectors (one for each wavelength) per additional dimension, but no additional lasers. Thus, our active phase-stabilization scheme scales very favorably and contributes to the excellent scalability of our whole approach to higher dimensions. Additionally, losses of 10 dB are handled by the current source and detection system. Although of relevance for the circuits's design, due to the nature of integrated circuits, coherence length and path difference are assumed not to be of major issue. However, a major stepping-stone toward high-dimensional MPs may be the decreasing process control with increasing circuit sizes and therefore reduced quality of the optical devices. Here, the major concern is the extinction ratio or visibility of the MZIs of the MP. Ultimately, low extinction ratios will reduce the MP's capability to realize arbitrary unitary transformations. In the following, we provide an estimate of this effect: The range of unitary operations implementable by the MP can be quantified. We define the "coverage" as the amount of unitary space "covered" by the MPs:

$$\mathrm{cov}_N = \frac{\prod_{i=1}^{N^2} \int_{\min \lambda_i}^{\max \lambda_i} \mathrm{d}\lambda_i J_N}{\int_{U(N)} \mathrm{d}U_N}, \tag{8}$$

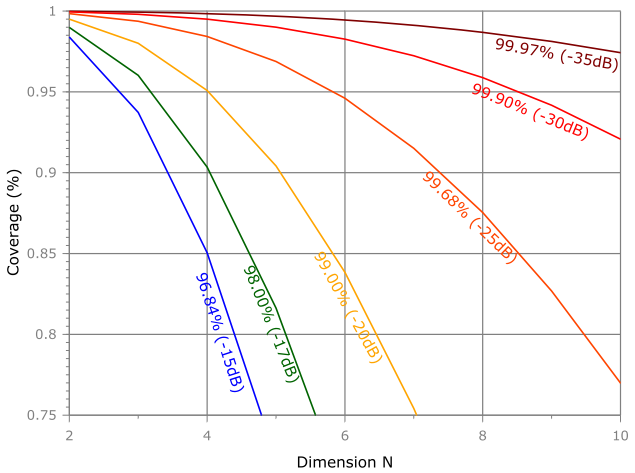

Fig. 4. Estimated coverage of the unitary space of an $N \times N$ MP of standard design [1,15]. Each plotted line assumes a different extinction ratio for all MZI units inside the MP. Phase shifters are assumed to cover the full range of phases, as has been experimentally verified. Currently, the characterized MP exhibits an average visibility of $(96.3 \pm 0.01)\%$ [extinction ratio of (14.2 ± 0.1) dB]. However, the current MP implementation has the a first/prototype run. Consequently, we are confident that next-generation devices tailored toward high extinction ratios will provide significant improvements. As an example, a 10-dimensional MP with an extinction ratio of −30 dB of all MZIs can realize more than 92% of the full unitary SU(10) space.

i.e., the ratio between the reachable unitary space given by all parameters and the full unitary space. The factor J_N represents the absolute value of the Jacobi determinant; see [27] for further details. The limits of λ_i are related to the range of reactivities (phases) implementable by each beam splitter (phase shifter). Analyzing a single MP, we estimate the coverage to $(96.3 \pm 0.01)\%$ of all unitary operations. Here, the limitation stems from the extinction ratios of the MZIs while phase shifters cover the full range $0 \ldots 2\pi$. Using the experimental results, we can further extrapolate the coverage of a higher-dimensional MP as illustrated in Fig. 4. Our results thus demonstrate that with experimentally feasible noise levels, moderate scalability of the devices is straightforward. Significant improvements can be expected with further tailoring of the next iterations of MP chips. Note, however, that using a MP of high coverage might not even be necessary as long as it can implement the sets of unitaries required for the experiment or quantum information protocol.

6. CONCLUSION

Combining previously developed devices, we have successfully implemented a system allowing for an exceptionally high degree of experimental control of an entangled two-qutrit, nine-dimensional photonic quantum system. An in-fiber source creates an entangled two-qutrit state of any amplitude and phase, while two MP devices realize any desired arbitrary local unitary transformation onto the quantum state. We demonstrate the quality of the system by performing a complete characterization of high-order perfect EPR correlations between two qutrits. Results are compared to theoretical prediction. Based on the performance of the current implementation, no direct technical limitations toward higher-dimensional systems become apparent. The source is directly extendible to two ququarts and could be implemented on-chip as well [19]. Compared to other state-of-the-art integrated circuits used in the area of telecommunications [28], higher-dimensional realizations of the MP are highly promising for quantum systems of dimension N. Further experiments may involve the generation and manipulation of entangled states [29], state discrimination [30], simulation of quantum logic [31], general optical simulation of spin-1 systems [15], an optical analog of the Stern–Gerlach experiment [15], tests of noncontextuality [4,15], realization of general positive operator valued measure (POVM) measurements [3032], or assistance in the search for the existence of complete sets of mutually unbiased basis (MUB) [33,34]. Additionally, the compatibility of the in-fiber source and MP to standard fiber networks at the Telecom wavelength will be of further interest for future applications. The design is a viable approach toward higher-dimensional quantum systems and offers great potential toward a higher level of integration and complexity of quantum systems.

European Commission (EC) (PIOF-GA-2012- 329851, SIQS grant no. 600645 EU-FP7-ICT, STREP "RAQUEL"); European Research Council (ERC) (227844); FWF (SFB F40, W1210-2); Generalitat de Catalunya (CIRIT Project No. 2014 SGR 966); MINECO (FIS2013-40627-P, JCI 2012-14155).

We thank Gerhard Hummer and the Austrian Institute of Technology for their contribution and technical help with the detection system.

REFERENCES

1. A. Laing, V. Scarani, J. G. Rarity, and J. L. O'Brien, "Reference-frame-independent quantum key distribution," Phys. Rev. A **82**, 012304 (2010).
2. D. Collins, N. Gisin, N. Linden, S. Massar, and S. Popescu, "Bell inequalities for arbitrarily high-dimensional systems," Phys. Rev. Lett. **88**, 040404 (2002).
3. I. Bengtsson, "Three ways to look at mutually unbiased bases," arXiv: quant-ph/0610216v1 (2006).
4. A. Cabello, E. Amselem, K. Blanchfield, M. Bourennane, and I. Bengtsson, "Proposed experiments of qutrit state-independent contextuality and two-qutrit contextuality-based nonlocality," Phys. Rev. A **85**, 032108 (2012).
5. S. Gröblacher, T. Jennewein, A. Vaziri, G. Weihs, and A. Zeilinger, "Experimental quantum cryptography with qutrits," New J. Phys. **8**, 75 (2006).
6. M. Huber and J. I. de Vicente, "Structure of multidimensional entanglement in multipartite systems," Phys. Rev. Lett. **110**, 030501 (2013).
7. A. Politi, J. C. F. Matthews, and J. L. O'Brien, "Shor's quantum factoring algorithm on a photonic chip," Science **325**, 1221 (2009).
8. M. Tillmann, B. Dakic, R. Heilmann, S. Nolte, A. Szameit, and P. Walther, "Experimental boson sampling," Nat. Photonics **7**, 540–544 (2013).
9. J. C. F. Matthews, A. Politi, A. Stefanov, and J. L. O'Brien, "Manipulation of multiphoton entanglement in waveguide quantum circuits," Nat. Photonics **3**, 346–350 (2009).
10. P. J. Shadbolt, M. R. Verde, A. Peruzzo, A. Politi, A. Laing, M. Lobino, J. C. F. Matthews, M. Thompson, and J. L. O'Brien, "Generating, manipulating and measuring entanglement and mixture with a reconfigurable photonic circuit," Nat. Photonics **6**, 45–49 (2011).
11. B. J. Metcalf, N. Thomas-Peter, J. B. Spring, D. Kundys, M. A. Broome, P. C. Humphreys, X.-M. Jin, M. Barbieri, W. S. Kolthammer, J. C. Gates, B. J. Smith, N. K. Langford, P. G. R. Smith, and I. A. Walmsley, "Multiphoton quantum interference in a multiport integrated photonic device," Nat. Commun. **4**, 1356 (2013).
12. A. Crespi, R. Osellame, R. Ramponi, D. J. Brod, E. F. Galvao, N. Spagnolo, C. Vitelli, E. Maiorino, P. Mataloni, and F. Sciarrino, "Integrated multimode interferometers with arbitrary designs for photonic boson sampling," Nat. Photonics **7**, 545–549 (2013).
13. Z. Chaboyer, T. Meany, L. G. Helt, M. J. Withford, and M. J. Steel, "Tuneable quantum interference in a 3D integrated circuit," arXiv:1409.4908 (2014).
14. D. Kaszlikowski and M. Zukowski, "Greenberger-Horne-Zeilinger paradoxes for N N-dimensional systems," Phys. Rev. A **66**, 1–6 (2002).
15. M. Zukowski, A. Zeilinger, and M. Horne, "Realizable higher-dimensional two-particle entanglements via multiport beam splitters," Phys. Rev. A **55**, 2564–2579 (1997).
16. M. Suda, C. Pacher, M. Peev, M. Dusek, and F. Hipp, "Experimental access to higher-dimensional entangled quantum systems using integrated optics," Quantum Inf. Process. **12**, 1915–1945 (2013).
17. R. Lapkiewicz, P. Li, C. Schaeff, N. K. Langford, S. Ramelow, M. Wiesniak, and A. Zeilinger, "Experimental non-classicality of an indivisible quantum system," Nature **474**, 490–493, (2011).
18. I. Bengtsson, W. Bruzda, A. Ericsson, J.-A. Larsson, W. Tadej, and K. Zyczkowski, "Mutually unbiased bases and Hadamard matrices of order six," J. Math. Phys. **48**, 052106 (2007).
19. C. Schaeff, R. Polster, R. Lapkiewicz, R. Fickler, S. Ramelow, and A. Zeilinger, "Scalable fiber integrated source for higher-dimensional path-entangled photonic quNits," Opt. Express **20**, 16145–16153 (2012).
20. M. Reck, A. Zeilinger, H. J. Bernstein, and P. Bertani, "Experimental realization of any discrete unitary operator," Phys. Rev. Lett. **73**, 58–61 (1994).
21. T. Shibata, M. Okuno, T. Goh, M. Yasu, M. Itoh, M. Ishii, Y. Hibino, A. Sugita, and A. Himeno, "Silica-based 16 16 optical matrix switch module with integrated driving circuits," in *Optical Fiber Communication Conference and International Conference on Quantum Information* (Optical Society of America, 2001), paper WR1.
22. M. Haruna and J. Koyama, "Thermo-optic waveguide interferometric modulator/switch in glass," IEE Proc, Part H **131**, 322–324 (1984).
23. A. Zeilinger, "General properties of lossless beam splitters in interferometry," Am. J. Phys. **49**, 882–883 (1981).
24. G. Weihs, M. Reck, H. Weinfurter, and A. Zeilinger, "All-fiber three-path Mach-Zehnder interferometer," Opt. Lett. **21**, 302–304 (1996).
25. S. Sohma, T. Watanabe, N. Ooba, M. Itoh, T. Shibata, and H. Takahashi, "Silica-based PLC Type 32 × 32 optical matrix switch," in *European Conference on Optical Communications (ECOC) 2006* (IEEE, 2006), pp. 1–2.
26. T. Goh, A. Himeno, M. Okuno, H. Takahashi, and K. Hattori, "High-extinction ratio and low-loss silica-based 8 × 8 strictly nonblocking thermooptic matrix switch," J. Lightwave Technol. **17**, 1192–1199 (1999).
27. Ch. Spengler, M. Huber, and B. C. Hiesmayr, "Composite parameterization and Haar measure for all unitary and special unitary groups," J. Math. Phys. **53**, 013501 (2012).
28. T. Goh, M. Yasu, K. Hattori, A. Himeno, M. Okuno, and Y. Ohmori, "Low loss and high extinction ratio strictly nonblocking 16 × 16 thermooptic matrix switch on 6-in wafer using silica-based planar lightwave circuit technology," J. Lightwave Technol. **19**, 371–379 (2001).
29. Y. Lim and A. Beige, "Multiphoton entanglement through a Bell-multiport beam splitter," Phys. Rev. A **71**, 062311 (2005).
30. M. Mohseni, A. M. Steinberg, and J. A. Bergou, "Optical realization of optimal unambiguous discrimination for pure and mixed quantum states," Phys. Rev. Lett. **93**, 200403 (2004).
31. N. Cerf, C. Adami, and P. Kwiat, "Optical simulation of quantum logic," Phys. Rev. A **57**, R1477–R1480 (1998).
32. G. N. M. Tabia, "Experimental scheme for qubit and qutrit symmetric informationally complete positive operator-valued measurements using multiport devices," Phys. Rev. A **86**, 062107 (2012).
33. M. Wiesniak, T. Paterek, and A. Zeilinger, "Entanglement in mutually unbiased bases," New J. Phys. **13**, 053047 (2011).
34. C. Spengler, M. Huber, S. Brierley, T. Adaktylos, and B. C. Hiesmayr, "Entanglement detection via mutually unbiased bases," Phys. Rev. A **86**, 022311 (2012).